Energy-function Based Pilot Protection Scheme for Hybrid UHVDC Transmission Applying Improved Hausdorff Distance

Zijiang Wang, Youping Fan, *Member*, *CSEE*, Ben Shang, and Yinbiao Shu, *Senior Member*, *IEEE*, *Fellow*, *CSEE*

***Abstract*—A hybrid UHVDC transmission system applying LCC as the rectifier and MMC as the inverter combines the advantages of both converter types, which makes this protection scheme more complicated. A new pilot protection scheme for a three-terminal hybrid DC transmission system applying energy functions is proposed. The energy function for LCC is applied to MMC to derive the energy level of the hybrid system. Furthermore, an improved Hausdorff distance (IHD) algorithm is proposed to detect the difference in energy levels between the normal and fault states. An abrupt change in energy level is characterized by IHD change rate. Time points at which the IHD change rate exceeds the threshold at converter stations are applied to determine the fault line and to estimate the fault section. The proposed protection scheme is then verified by a simulation model of the Wudongde ±800 kV three-terminal hybrid UHVDC transmission project. The appropriate sampling frequency is selected for a real-time calculation, and the threshold is selected considering the effect of noise. Results show the proposed scheme can identify and trip fault lines quickly and effectively, even for a 600 Ω grounding fault. Other waveshape similarity algorithms are compared and analyzed. Compared with existing protection schemes, the proposed scheme transmits less data to improve communication speed and reliability.**

***Index Terms*—Energy function, Hausdorff distance, pilot protection, UHVDC transmission.**

I. Introduction

THE development of a modern society is usually accompanied by an increase in electricity demand. An increasing number of devices have been connected on a large scale in recent years, which has made the construction, operation, and maintenance of power systems more difficult [1], [2]. To reduce the loss during long-distance transmission, ultra-high voltage direct current (UHVDC) transmission technology has gradually become a good choice due to its smaller transmission corridor, higher transmission efficiency, and lower cost [3]. Among the different types of UHVDC transmission technologies, a line commutated converter (LCC) is relatively mature and low-cost and is widely applied in UHVDC transmission projects. Despite its many advantages, continuous commutation failure may occur when applying an LCC as the inverter [4]–[6]. With the development of large-capacity, full-controlled power electronic devices, flexible DC transmission systems applying voltage source converters (VSCs) with higher flexibility for controlling active power and reactive power have been developing rapidly. The modular multilevel converter (MMC) developed from traditional VSC reduces switching frequencies along with harmonics, which makes it promising for long-distance UHVDC transmission [7]–[10]. However, application of MMC for large-capacity power transmission significantly increases construction and operation costs, which is why the LCC-MMC hybrid scheme was proposed. By combining LCC with MMC, the hybrid scheme applied LCC as the rectifier and MMC as the inverter can transmit large capacity power without the problem of continuous commutation failure and reduce construction cost. The hybrid scheme combines the advantages of both converters and fault clearance more economically [11]. The currently completed hybrid three-terminal DC transmission project in Wudongde was the first application of this hybrid UHVDC transmission scheme, which achieved 8000 MW of power delivery on the Yunnan side through LCC and 5000 MW and 3000 MW of power delivery on the Guangdong and Guangxi sides through MMC, respectively [12], [13].

With the rapid development of UHVDC transmission systems, protecting DC lines has become a key issue to be addressed. Structure of the hybrid UHVDC transmission system is different from traditional UHVDC transmission system with one type of converter, which means conventional protection methods are not fully suitable. Traveling wave protection is the main protection scheme for the UHVDC transmission. With distortion and attenuation of the traveling wave by special T areas and long-distance transmission lines, sensitivity of traveling wave protection for high resistance fault is reduced [12]. The traveling wave protection scheme locates the fault line by the traveling wave generated by line boundary elements such as smoothing reactors and DC filters. However, there are no DC filters at the VSC side and the reactor of the VSC is much smaller than the LCC [14], [15], which makes it difficult to determine the fault line. To solve the problems mentioned above, the ratio of the time-domain transient voltage in different sampling periods was analyzed

Manuscript received March 3, 2022; revised July 3, 2022; accepted July 25, 2022. Date of online publication March 3, 2023; date of current version February 5, 2024. This work was supported by the Science and Technology Project of China Southern Power Co., Ltd. (CGYKJXM20180508).

Z. J. Wang, Y. P. Fan (corresponding author, email: ypfan@whu.edu.cn), B. Shang, and Y. B. Shu are with the School of Electrical Engineering and Automation, Wuhan University, Wuhan 430072, China, and also with the Institute of Next Generation Power Systems & International Standards, Wuhan University, Wuhan 430072, China.

DOI: 10.17775/CSEEJPES.2022.01330

2096-0042 © 2022 CSEE. This is an open access article under the CC BY-NC-ND license (http://creativecommons.org/licenses/by-nc-nd/4.0/).

and utilized [12] to reduce the effects of high resistance and T area. However, in practical engineering, acquisition of high-frequency components is difficult, which brings higher requirements of computational speed and storage capacity. The method was verified by simulation, but computational and transmission delays in practical engineering were not discussed and analyzed. The first peak time of line-mode fault component voltage (FPTV) was analyzed and proved to be immune to the effects of fault resistance and fault type [16], and the difference of FPTV between internal and external faults was applied to locate the faults. Different converter types and boundary elements were considered [16], but some faults can't be distinguished in the case without boundaries at line ends. With higher sensitivity for high resistance faults and without requirements for boundary elements, pilot protection has been applied in a hybrid DC transmission system. Polarity characteristics of the current and voltage fault components at the rectifier and inverter were analyzed and utilized for protection [17]. The method is only applicable in a two-terminal hybrid DC transmission system. Characteristics of fault components are much more complicated in multi-terminal DC (MTDC) systems with 3 or more terminals, and the fault is difficult to locate only by polarities of fault components. Fault direction discrimination criteria were proposed [18], and the fault was located with direction information at both ends of the line. The direction discrimination criteria proposed are based on traveling wave characteristics, and criteria need to be modified when system topologies change.

The Hausdorff distance (HD) was an algorithm to analyze waveshape similarity between two different waves. The HD reflects the difference between the normal state and the abnormal state of the power system in a short time window, which is suitable for UHVDC protection. However, the original HD algorithm is sensitive to noise and abnormal data, which can lead to significantly larger values. To solve this shortcoming, some improved HD algorithms are proposed. In [19], [20], ratios of the 2 directed HDs were calculated and compared with the set threshold to select the true maximum distance. In [21], a partial HD (PHD) algorithm was proposed. When abnormal data emerged, the 6th largest value was selected as the maximum distance to remove the abnormal data. Details of these improved HD algorithms are introduced and discussed in Section IV.

For conventional protection schemes, protection schemes using voltage for judgment are easily influenced by fault resistance [22]. Differential current protection can detect the high resistance fault but has longer time delay to avoid influence of capacitive current [23]. Overcurrent protection is not suitable in MTDC systems, because high-level fault current may cause protection maloperation of the non-faulted line [24]. There is a need to find a new protection criterion to overcome these shortcomings. Energy function, which is an approach for quantifying energy level of a power system, has been applied to analyze stability of AC transmission systems [25], [26]. For DC transmission systems, the energy function was first mentioned in [27], proposing an energy function based on the structure-preserving model to estimate transient energy of a DC system. For the construction method, a numerical method for constructing energy functions based on a detailed model of AC and DC systems was proposed and verified in [28]. To improve accuracy of stability prediction results, the transient energy function that can represent the dynamic characteristics of AC/DC systems was given in [1]. For the protection scheme for UHVDC transmission, energy level is selected as the action criterion. A method for calculating low-frequency energy difference between two sides of DC lines, which are immune to interference of lightning and sensitive enough for high-resistance grounding faults, was proposed in [29] to identify the fault pole and external or internal faults. In this paper, a pilot protection scheme using energy level as the criterion has been proposed, which can detect a high resistance fault in a short time.

As discussed above, conventional DC transmission systems' traveling wave protection schemes have shortcomings when applied in hybrid DC transmission systems, and conventional protection schemes are not fully applicable. Therefore, research on a protection scheme of the hybrid DC transmission system is needed. In this paper, energy function combined with waveshape similarity algorithm is applied to construct pilot protection for UHVDC transmission systems. A pilot protection scheme for a three-terminal hybrid UHVDC transmission system is proposed, which is applied as backup protection and an auxiliary criterion to identify the fault line and estimate the fault section. For the three-terminal hybrid UHVDC transmission system, the energy function for MMC is constructed based on the energy function for LCC. Then, energy levels for three converter stations are derived. An improved Hausdorff distance (IHD) algorithm is proposed to avoid incorrect results caused by abnormal data, which may lead to protection maloperation. A pilot protection scheme using the IHD algorithm to calculate the energy level difference of different stations at normal or fault state is proposed. Abrupt change in energy level is characterized by the IHD change rate. Time points at which the IHD change rates exceed the threshold are collected and compared to determine the fault line and estimate the fault section.

The rest of the sections are arranged as follows: In Section II, the detailed process for constructing energy functions is introduced. In Section III, the IHD algorithm is introduced and applied in the proposed pilot protection scheme. In Section IV, the protection scheme proposed is verified by a simulation model of the Wudongde $\pm$800 kV three-terminal hybrid UHVDC transmission project built in PSCAD/EMTDC. The IHD algorithm is then compared and analyzed with the absolute distance algorithm and different HD algorithms, which proves the advantages of the IHD algorithm. A comparison of the energy level criterion and single state parameter criterion illustrates the advantages of the protection scheme by applying energy functions. Communication delay of the proposed protection scheme is discussed and compared with existing schemes. The main contributions are concluded in Section V.

II. Construction of the Energy Function for a Hybrid UHVDC Transmission System

A. Hybrid UHVDC Transmission System Model

For the hybrid DC transmission system shown in Fig. 1,

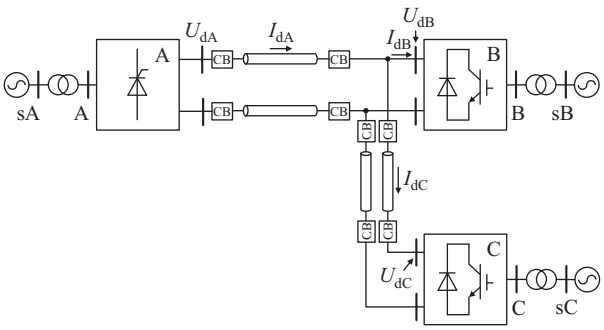

Fig. 1. Structure of the LCC-MMC three-terminal hybrid UHVDC transmission system.

Station A is an LCC rectifier station, while Station B and C are MMC inverter stations. CB is the DC circuit breaker equipped on the DC line, and A, sA, B, sB, C and sC are bus labels of the AC system. For the system shown in Fig. 1, the voltage and current of the UHVDC system can be expressed as (1).

$$\begin{cases} U_{\mathrm{dA0}} = 1.35 U_{\mathrm{A}} \cos\alpha \\ U_{\mathrm{dA}} = N_{\mathrm{A}}(U_{\mathrm{dA0}} - 3 I_{\mathrm{dA}} X_{\mathrm{A}}/\pi) \\ I_{\mathrm{dA}} = (U_{\mathrm{dA}} - U_{\mathrm{dB}})/R_{\mathrm{AB}} \\ I_{\mathrm{dC}} = (U_{\mathrm{dB}} - U_{\mathrm{dC}})/R_{\mathrm{BC}} \\ I_{\mathrm{dB}} = I_{\mathrm{dA}} - I_{\mathrm{dC}} \end{cases} \tag{1}$$

where X_{A} is the commutation reactance of Station A, N_{A} is the number of groups of six-pulse converters in Station A, U_{A} is voltage amplitude of Bus A, α is firing angle, U_{dA0} is DC voltage of Station A without a load, U_{dA}, U_{dB}, U_{dC}, I_{dA}, I_{dB}, and I_{dC} are DC voltage and DC current of Station A, Station B and Station C, respectively, and R_{AB} and R_{BC} are resistances of Line AB and Line BC, respectively. The power of Station A can be obtained according to (2).

$$\begin{cases} P_{\mathrm{A}} = U_{\mathrm{dA}} I_{\mathrm{dA}} \\ Q_{\mathrm{A}} = P_{\mathrm{A}} \tan\varphi_{\mathrm{A}} \\ \varphi_{\mathrm{A}} = \arccos(U_{\mathrm{dA}}/1.35 N_{\mathrm{A}} U_{\mathrm{A}}) \end{cases} \tag{2}$$

Power expressions of Station B and Station C are shown in (3) and (4), respectively.

$$\begin{cases} P_{\mathrm{B}} = U_{\mathrm{B}} U_{\mathrm{sB}} \sin\delta_{\mathrm{B}}/X_{\mathrm{B}} \\ Q_{\mathrm{B}} = U_{\mathrm{B}}(U_{\mathrm{B}} - U_{\mathrm{sB}} \cos\delta_{\mathrm{B}})/X_{\mathrm{B}} \end{cases} \tag{3}$$

$$\begin{cases} P_{\mathrm{C}} = U_{\mathrm{C}} U_{\mathrm{sC}} \sin\delta_{\mathrm{C}}/X_{\mathrm{C}} \\ Q_{\mathrm{C}} = U_{\mathrm{C}}(U_{\mathrm{C}} - U_{\mathrm{sC}} \cos\delta_{\mathrm{C}})/X_{\mathrm{C}} \end{cases} \tag{4}$$

where U_{B} and U_{C} are fundamental line voltage amplitudes of Bus B and C, respectively, U_{sB} and U_{sC} are line voltage amplitudes of Bus sB and sC, respectively, X_{B} and X_{C} are fundamental reactance of transformers in Station B and Station C, respectively, and δ_{B} and δ_{C} are voltage phase angle differences of Station B and Station C.

B. Construction of the Energy Function

First, the energy function of Station A is constructed by referring to the construction approach for DC systems given in [27] and [28]. Considering universality of the energy functions constructed, the construction approach without assumption is adopted, which can be applied in more situations. Assuming $B_{\mathrm{A}} = \pi/3X_{\mathrm{A}}$, we can obtain (5) from (1):

$$U_{\mathrm{dA}} = \frac{N_{\mathrm{A}}(U_{\mathrm{dB}} + B_{\mathrm{A}} R_{\mathrm{AB}} U_{\mathrm{dA0}})}{B_{\mathrm{A}} R_{\mathrm{AB}} + N_{\mathrm{A}}} \tag{5}$$

According to (2), P_{A} and Q_{A} can be derived by measuring DC current I_{dA}; then, energy level of Station A can be calculated as:

$$V_{\mathrm{A}} = \int_{\delta_{\mathrm{A0}}}^{\delta_{\mathrm{A}}} P_{\mathrm{A}} \mathrm{d}\delta + \int_{U_{\mathrm{A0}}}^{U_{\mathrm{A}}} Q_{\mathrm{A}} \mathrm{d}u \tag{6}$$

where U_{A0} and δ_{A0} are voltage amplitude and its phase angle, respectively, of Station A without a load when the system operates normally. Since (6) is complex, it is difficult to find a concise analytical expression, so the trapezoidal integral method is applied to approximate the numerical solution of the integral equation to represent the energy level of Station A. Assuming the number of sampling points is N, the integration result of (6) can be expressed as:

$$\begin{aligned} V_{\mathrm{A}} = {} & \frac{\delta_{\mathrm{A}} - \delta_{\mathrm{A0}}}{2N} \sum_{n=1}^{N} [P_{\mathrm{A}}(\delta_n) + P_{\mathrm{A}}(\delta_{n+1})] \\ & + \frac{U_{\mathrm{A}} - U_{\mathrm{A0}}}{2\ N} \sum_{n=1}^{N} [Q_{\mathrm{A}}(U_n) + Q_{\mathrm{A}}(U_{n+1})] \end{aligned} \tag{7}$$

Second, for stations that adopted MMC, taking Station B as an example, the energy function is constructed by extending the construction method for LCC. The energy function is then constructed by replacing active power, reactive power, voltage amplitude, and its angle with corresponding values of MMC according to (3). Then, the energy function of Station B can be derived as:

$$\begin{aligned} V_{\mathrm{B}} &= \int_{\delta_{\mathrm{B0}}}^{\delta_{\mathrm{B}}} P_{\mathrm{B}} \mathrm{d}\delta + \int_{U_{\mathrm{B0}}}^{U_{\mathrm{B}}} Q_{\mathrm{B}} \mathrm{d}u \\ &= -U_{\mathrm{B}} U_{\mathrm{sB}} \cos\delta/X_{\mathrm{B}}|_{\delta_{\mathrm{B0}}}^{\delta_{\mathrm{B}}} \\ &\quad + u^2(2u - 3U_{\mathrm{sB}} \cos\delta_{\mathrm{B}})/6X_{\mathrm{B}}|_{U_{\mathrm{B0}}}^{U_{\mathrm{B}}} \end{aligned} \tag{8}$$

where U_{B0} and δ_{B0} are voltage amplitude and phase angle difference, respectively, of Station B when the system operates normally. The energy function of Station C can therefore be derived according to the energy function of Station B.

III. Protection Principles and Protection Schemes

A. Improved Hausdorff Distance Algorithm by Removing Abnormal Data

1) Original HD Algorithm

HD is a quantitative way to characterize the similarity between two waveforms, which uses an Euclidean norm of sets of waveform points to represent differences between waveforms. We assume the two-dimensional point sets consisting of waveforms 1 and 2 can be represented as:

$$\begin{cases} W_1 = \{(t_1, f_1(t_1)), \cdots, (t_n, f_1(t_n))\} \\ W_2 = \{(t_1, f_2(t_1)), \cdots, (t_n, f_2(t_n))\} \end{cases} \tag{9}$$

where t is time point and f is a function of t. The original HD can be calculated as follows. First, calculate the distance D_i, which is the distance of a certain point $(t_i, f_1(t_i)) \in W_1$ from the nearest point $(t_\mathrm{m}, f_2(t_\mathrm{m})) \in W_2$, as:

$$\begin{aligned} D_i &= \sqrt{(t_i - t_\mathrm{m})^2 + (f_1(t_i) - f_2(t_\mathrm{m}))^2} \\ &\le \sqrt{(t_i - t_k)^2 + (f_1(t_i) - f_2(t_k))^2} \end{aligned} \tag{10}$$

where $1 \le k \le n$. Then, the directed HD from W_1 to W_2 can be calculated as:

$$h_{12} = \max\{D_i | 1 \le i \le n\} \tag{11}$$

The directed HD from W_2 to W_1 can be calculated similarly, as:

$$h_{21} = \max\{D_j | 1 \le j \le n\} \tag{12}$$

Then, ordinary HD can be obtained as:

$$H = \max\{h_{12}, h_{21}\} \tag{13}$$

Equation (13) means the larger value between two directed HDs is the HD of two-point sets.

2) IHD Algorithm

In the process of data collection, there will be individual abnormal data resulting in higher energy levels, which may lead to higher HD results. An improved algorithm is proposed here that can effectively avoid influence caused by abnormal data, and the specific procedure is as follows.

First, all elements of D_i are ranked in order from largest to smallest. Then we derive new dataset $\{D_{\mathrm{rank}i} | 1 \le i \le n\}$, where D_{rank1} is the largest element among the dataset and $D_{\mathrm{rank}n}$ is the smallest one.

Second, calculate judgment parameters $G(D_{\mathrm{rank}i})$ for every element in the dataset $\{D_{\mathrm{rank}i} | 1 \le i \le n\}$ and make a judgment, as follows:

$$G(D_{\mathrm{rank}i}) = \frac{D_{\mathrm{rank}i} - D_{\mathrm{rank}(i+1)}}{D_{\mathrm{rank}(i+1)} - D_{\mathrm{rank}(i+2)}} > G_{\mathrm{gate}} \tag{14}$$

where 'G_{gate}' is the manually set threshold value and can be adjusted to a value larger than 1 according to request of the project. In the case mentioned in this paper, G_{gate} is set to 100 because the difference of each element in the set is lower than 0.01 p.u. under normal states, while abnormal data are set higher than 1 p.u. If the G parameter of the maximum element $G(D_{\mathrm{rank1}})$ exceeds the G_{gate}, then value of D_{rank1} is abnormal. Then, G parameter of the next element D_{rank2} is checked. Until we find the first $D_{\mathrm{rank}i}$ whose G parameter is below the gate, this value is output as h_{12}. Similarly, we can obtain the value of h_{21} and finally obtain the IHD value. The IHD algorithm proposed here is appropriate for cases when several abnormal data points emerge and can avoid protection against false line trips.

B. Fault Analysis Based on Equivalent Circuits for Three-terminal Hybrid Systems

To analyze the fault on Line AB, a three-terminal hybrid DC transmission model shown in Fig. 1 can be further simplified, as shown in Fig. 2.

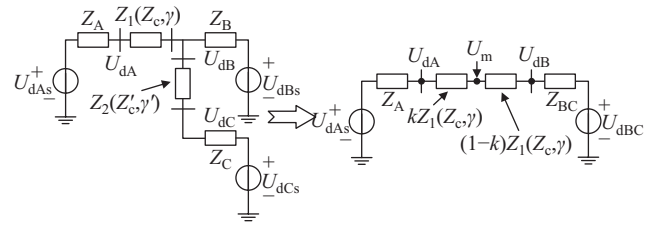

Fig. 2. Simplified equivalent circuit of the three-terminal DC transmission system.

Where k is a number ranging from 0 to 1 to split Line AB into two sections, U_m is voltage of the splitting point under normal operation, $Z_1(Z_\mathrm{c}, \gamma)$ and $Z_2(Z'_\mathrm{c}, \gamma')$ represent line impedances of Line AB and Line BC [30], and distributed parameters of DC lines Z_c and γ represent surge impedance and propagation constant, respectively. For simplicity, distributed parameters are not displayed in the figures or equations in the following analysis. U_aAs, U_dBs, and U_dCs represent equivalent DC voltages of the three converters, Z_BC and U_dBC represent equivalent impedance and DC voltage after merging Station B and Station C respectively, and Z_A, Z_B, Z_C, Z_BC, and U_dBC are calculated as (15).

$$\begin{cases} Z_\mathrm{A} = R_\mathrm{A} + \mathrm{j}\omega L_\mathrm{A} + \mathrm{j}\omega L_\mathrm{s} \\ Z_\mathrm{B} = R_\mathrm{B} + \mathrm{j}\omega L_\mathrm{B} + \mathrm{j}\omega L_\mathrm{s} \\ Z_\mathrm{C} = R_\mathrm{C} + \mathrm{j}\omega L_\mathrm{C} + \mathrm{j}\omega L_\mathrm{s} \\ Z_\mathrm{BC} = \frac{Z_\mathrm{B}(Z_\mathrm{C}+Z_2)}{Z_\mathrm{B}+Z_\mathrm{C}+Z_2} \\ U_\mathrm{dBC} = \frac{(Z_\mathrm{C}+Z_2)U_\mathrm{dBs}+Z_\mathrm{B}U_\mathrm{dCs}}{Z_\mathrm{B}+Z_\mathrm{C}+Z_2} \end{cases} \tag{15}$$

where R_x and L_x (x = A, B, C) represent equivalent resistance and impedance of converters and DC filters in three stations, L_s represents equivalent impedance of the smoothing reactor. Voltages of three points shown in Fig. 2 under normal operation are calculated as (16).

$$\begin{cases} U_\mathrm{dA} = \frac{(Z_1+Z_\mathrm{BC})U_\mathrm{dAs}+Z_\mathrm{A}U_\mathrm{dBC}}{Z_\mathrm{A}+Z_1+Z_\mathrm{BC}} \\ U_\mathrm{dB} = \frac{(Z_\mathrm{A}+Z_1)U_\mathrm{dBC}+Z_\mathrm{BC}U_\mathrm{dAs}}{Z_\mathrm{A}+Z_1+Z_\mathrm{BC}} \\ U_\mathrm{m} = \frac{(1-k)Z_1U_\mathrm{dAs}+(Z_\mathrm{A}+kZ_1+Z_\mathrm{BC})U_\mathrm{dBC}}{Z_\mathrm{A}+Z_1+Z_\mathrm{BC}} \end{cases} \tag{16}$$

When a fault occurs at a point between two sections of Line AB, suppose R_f is grounding resistance, and the superimposed fault-component network is obtained based on the superposition principle, which is shown in Fig. 3, where U_dAf and U_dBf are voltage changes at both ends of Line AB caused by the fault, U_f is voltage change of the fault point on the line.

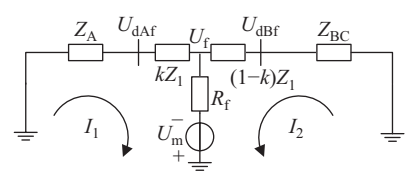

Fig. 3. Superimposed fault-component network of Line AB fault.

We apply KVL in two loops shown in Fig. 3 to obtain (17).

$$\begin{cases} U_\mathrm{m} = (Z_\mathrm{A} + kZ_1 + R_\mathrm{f})I_1 + R_\mathrm{f}I_2 \\ U_\mathrm{m} = [Z_\mathrm{A} + (1-k)Z_1 + R_\mathrm{f}]I_2 + R_\mathrm{f}I_1 \end{cases} \tag{17}$$

I_1 and I_2 are solved from (17) as follows:

$$\begin{cases} I_1 = \frac{U_{\mathrm{m}}[Z_{\mathrm{BC}}+(1-k)Z_1]}{R_{\mathrm{f}}(Z_{\mathrm{A}}+Z_1+Z_{\mathrm{BC}})+(Z_{\mathrm{A}}+kZ_1)[Z_{\mathrm{BC}}+(1-k)Z_1]} \\ I_2 = \frac{U_{\mathrm{m}}(Z_{\mathrm{A}}+kZ_1)}{R_{\mathrm{f}}(Z_{\mathrm{A}}+Z_1+Z_{\mathrm{BC}})+(Z_{\mathrm{A}}+kZ_1)[Z_{\mathrm{BC}}+(1-k)Z_1]} \end{cases} \tag{18}$$

Then, U_{dAf} and U_{dBf} are obtained as (19).

$$\begin{cases} U_{\mathrm{dAf}} = -I_1 Z_{\mathrm{A}} \\ U_{\mathrm{dBf}} = -I_2 Z_{\mathrm{BC}} \\ U_{\mathrm{f}} = (I_1+I_2)R_{\mathrm{f}} - U_{\mathrm{m}} \\ \quad = -\frac{U_{\mathrm{m}}[Z_{\mathrm{BC}}+(1-k)Z_1](Z_{\mathrm{A}}+kZ_1)}{R_{\mathrm{f}}(Z_{\mathrm{A}}+Z_1+Z_{\mathrm{BC}})+(Z_{\mathrm{A}}+kZ_1)[Z_{\mathrm{BC}}+(1-k)Z_1]} \end{cases} \tag{19}$$

According to (18) and (19), when $R_{\mathrm{f}} \to +\infty$, there are $U_{\mathrm{f}} \to 0$, $U_{\mathrm{dAf}} \to 0$, and $U_{\mathrm{dBf}} \to 0$, U_{dA} and U_{dB} will not change. When $R_{\mathrm{f}} \to 0$, there is $U_{\mathrm{f}} \to -U_{\mathrm{m}}$, and

$$\begin{cases} U_{\mathrm{dAf}} \to -\frac{Z_{\mathrm{A}}}{Z_{\mathrm{BC}}+(1-k)Z_1}U_{\mathrm{m}} \\ U_{\mathrm{dBf}} \to -\frac{Z_{\mathrm{BC}}}{Z_{\mathrm{A}}+kZ_1}U_{\mathrm{m}} \end{cases}$$

U_{dA} and U_{dB} will change most in this case. It can be concluded that voltages at both ends of Line AB drop when a fault occurs on Line AB, and the change value decreases with the increase of R_{f}.

When a fault occurs on Line BC, the superimposed fault-component network is obtained as Fig. 4.

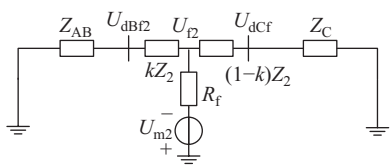

Fig. 4. Superimposed fault-component network of Line BC fault.

In Fig. 4, Z_{AB} is equivalent impedance after merging Station A and Station B, U_{dBf2} and U_{dCf} represent voltage changes at both ends of Line BC caused by the fault, and U_{f2} is voltage change of the fault point on Line BC. Therefore, expressions of U_{dBf2} and U_{dCf} are in the same form as (18) and (19), and detailed results are not shown here.

As voltage drops because of the grounding fault, the upper limit of integration of the energy function will change, as shown in (5)–(8). Energy level calculated becomes higher, resulting in a difference relative to normal state, and corresponding IHD will be significantly higher. Based on changes in the system state quantities following a fault obtained above, a protection scheme can be designed accordingly.

C. Protection Principle and Fault Location Estimation

A protection principle is designed according to the time point of an abrupt IHD change. Based on conclusions derived in the previous section, when a grounding fault occurs, line voltages of the converter stations at both ends of the fault line decrease. Voltage reduction can lead to changes in grid voltage and transmitted power, which can thus result in an energy level change. Changes in the energy level waveform can be quickly detected and quantified by applying the IHD method. When a fault occurs at different points, the change moments of the IHD values of each converter station are different due to long transmission lines. The change amount of the IHD at the same moment is applied to determine the fault pole. The IHD value of the fault pole changes more than that of the normal pole. Then, the fault line, and even the fault section of the line, can be determined based on the relationship of the change moment, the length of the line, and transmission speed of voltage and current signal. An action signal is sent accordingly.

The abrupt change in energy level can be characterized by the change rate of IHD and corresponding threshold. Fault location can be determined based on the time difference between the change rate exceeding the threshold of each converter station. For a three-terminal DC transmission system shown in Fig. 1, assuming Line AB is longer than Line BC and the fault is located at exit line of Station B, the time difference between the abrupt change of Station A and Station C is calculated as $(l_{\mathrm{AB}} - l_{\mathrm{BC}})/c$, where l_{AB} and l_{BC} are lengths of Line AB and Line BC respectively, c is transmission speed of voltage and current signal, i.e., 3×10^8m/s. Then, fault line selection criteria are obtained as (20) for Line AB and (21) for Line BC.

$$t_{\mathrm{C}} \geq t_{\mathrm{A}} - \frac{l_{\mathrm{AB}} - l_{\mathrm{BC}}}{c} + \Delta t \tag{20}$$

$$t_{\mathrm{A}} \geq t_{\mathrm{C}} + \frac{l_{\mathrm{AB}} - l_{\mathrm{BC}}}{c} + \Delta t \tag{21}$$

where Δt is dead time to avoid the time overlap, t_{A} and t_{C} are time points of the abrupt change in IHD values of Station A and Station C, respectively. It should be noted that (20) and (21) only show the ideal time difference threshold, and the difference in communication time delay needs to be further considered for actual engineering applications.

In addition, the fault section of the line can be estimated based on the time difference of the abrupt change in IHD between converter stations at both ends of the line. Assuming when a fault occurs on Line AB, the distance x_{A} of the fault point from Station A can be estimated according to (22).

$$x_{\mathrm{A}} = \frac{l_{\mathrm{AB}} - c(t_{\mathrm{B}} - t_{\mathrm{A}} + 2t_{\mathrm{d}})}{2} \tag{22}$$

where t_{A} and t_{B} are the time points of the abrupt change in IHD values of Station A and Station B, respectively, t_{d} is the sampling interval.

On one hand, the time difference between change rates in IHD of Station A and Station C that exceed the threshold is applied to identify the fault line. On the other hand, the time difference between adjacent stations is applied to estimate the fault point on the fault line. The proposed protection scheme applies local data to generate and transmit action signals in order to determine the fault line and the fault section of the line, which can reduce the amount of data transmitted, and thus improve reliability.

D. Influence Analysis of the Distributed Capacitance

For long-distance UHVDC transmission lines, current magnitudes will increase because of distributed capacitance, which may result in maloperation of traditional protection if increased capacitance current is not compensated properly. When designing the protection scheme in this paper, currents of the normal state at Station A, Station B, and Station C, i.e.,

I_{dA}, I_{dB}, and I_{dC} respectively, are selected as base values to calculate normal state energy level. Currents mentioned above contain increased current caused by distributed capacitance. Thus, the derived energy level has already taken effect of the capacitance current into account. When comparing the energy level between fault state and normal state using the proposed IHD algorithm, the relative difference in energy level is compared. The difference becomes more obvious because of amplification by distributed capacitance, which is beneficial for fault detection.

E. Identification of Lightning Interference

Lightning strokes can lead to maloperation of the protection system, which may result in unnecessary UHVDC system outages. Therefore, it is critical to determine whether abnormal data is generated by grounding fault or by lightning interference. Grounding fault increases current significantly, but in most cases, a lightning stroke reduces current, which can be applied as the criterion to discriminate between lightning interference and grounding fault. There are other methods to identify lightning interference. In [31], a high-speed method was proposed to distinguish differences between lightning interference and lightning fault. The method analyzes the reverse voltage traveling wave characteristics to distinguish the difference between different fault types. For the proposed protection scheme, the initial change direction of the current is collected to exclude cases of lightning interference.

F. Overall Process of Protection

The proposed protection scheme focuses on DC line grounding faults. Directional elements are needed at both ends of DC lines to discriminate between AC line fault and DC line fault. For DC line fault, the overall protection process is shown in Fig. 5, where the dashed lines indicate the action signal transmitted to the DC circuit breaker. The parameters, including values of N_{A}, R_{AB}, R_{BC}, X_{A}, X_{B}, X_{C}, and normal energy level data, need to be input first. Voltage, current, and voltage phase angle data of each converter station are collected in order to calculate the energy level based on the energy function constructed. The IHD value can be calculated based on normal energy level data and real-time energy level. The change rate is obtained, and the time point where the change rate exceeds threshold is recorded. Finally, according to the time difference where the change rates of Station A and Station C exceed threshold, the fault line is determined and tripped.

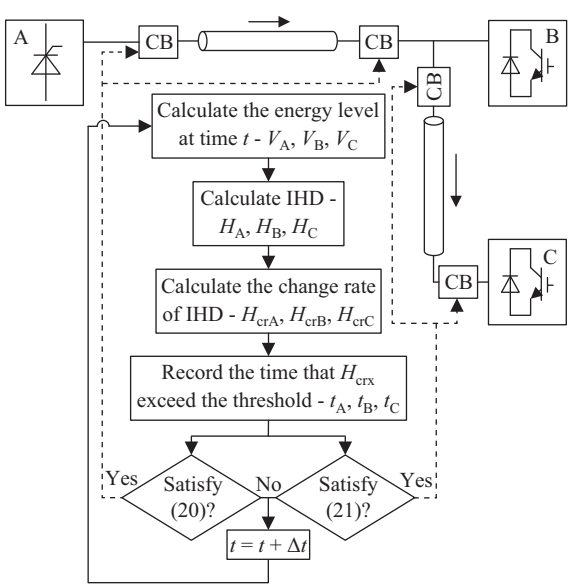

Fig. 5. Logic flow chart of protection.

IV. Case Studies

To test effectiveness of the protection scheme proposed in this paper, the Wudongde ±800 kV three-terminal hybrid UHVDC model shown in Fig. 1 is built in PSCAD/EMTDC. System parameters are set according to the actual project. The DC transmission line is set as a frequency-dependent model. The length of Line AB is 932 km, and the length of Line BC is 557 km. All mentioned faults are set to occur at 0 ms. Simulation is run on an Intel Core i5-10400 2.90 GHz computer with 16 GB of RAM.

A. Selection of Sampling Frequency

Sampling frequency is directly related to the amount of data collected and the speed of calculation. When applying a higher sampling frequency, the amount of data collected is larger, and the calculation speed required is higher, but the fault can be detected earlier. In contrast, it is easier to achieve real-time calculations on lower sampling frequency because of the lower amount of data, but the time point of detecting the fault lags. In this section, the midpoint fault on Line AB is set as an example to test sampling frequencies. Calculation time, peak time point, and other data are collected and compared to select the appropriate sampling frequency for simulation. Data from 1 kHz to 50 kHz are shown in Table I, and the IHD change rate figures for 25 kHz, 10 kHz, 5 kHz, and 1 kHz are shown in Fig. 6. The unit of the IHD change rate is p.u./ms.

TABLE I
Comparison of Different Sampling Frequencies

f_{s} (kHz)	t_{d} (ms)	t_{c} (ms)	Ratio of t_{d} to t_{c}	t_{p} (ms)
50	0.02	361.634	18 081.7	1.80
25	0.04	57.247	1 431.2	1.84
10	0.1	5.912	59.1	2.00
5	0.2	1.269	6.3	2.20
1	1	0.095	0.1	4.00

In Table I, f_{s} represents the sampling frequency, t_{d} represents sampling interval, i.e., $1/f_{\mathrm{s}}$, t_{c} represents calculation time, and t_{p} represents the time point of first detected peak. The ratio of t_{d} to t_{c} is applied to estimate the required speed multiple to achieve real-time calculation. Based on data in Table I, real-time calculation of 10 kHz sampling can be achieved when calculation speed is increased by approximately 60 times. Results are obtained using MATLAB R2021a on an ordinary desktop computer, whose calculation speed and efficiency are much lower than those of the computers applied in engineering practice. We suppose the real-time calculation can be achieved on 10 kHz by upgrading the hardware and optimizing the algorithm. Therefore, 10 kHz is selected as

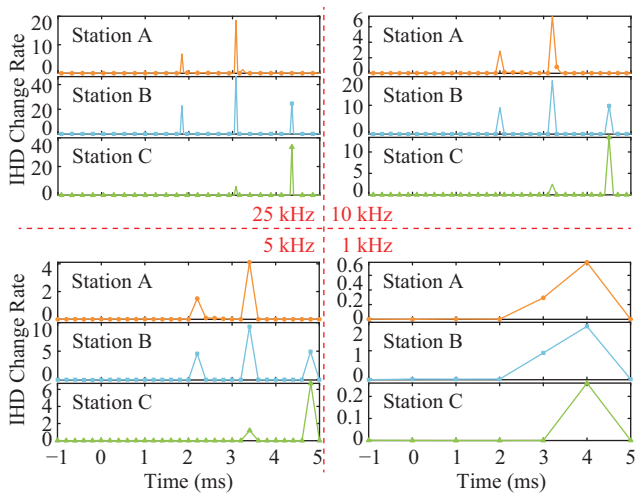

Fig. 6. IHD change rate figure of the different sampling frequencies.

the sampling frequency for the following simulation, and the sampling interval t_{d} is 0.1 ms.

B. Determination of the Threshold and the Criteria

Since IHD value is much less when a high-impedance grounding fault occurs, IHD change rate is also less than the grounding fault without impedance. The threshold is selected under an extreme state with a grounding resistance of 600 Ω, which can ensure the protection system can detect the fault, even in the event of a high impedance grounding situation. In addition, influence of noise should also be considered when selecting the threshold. The Gaussian noise signal with a 40 dB signal-to-noise ratio (SNR) is added to the original energy data. Change rate peak values caused by the IHD change and by the influence of noise are shown in Table II. Fault point numbers are shown in Fig. 7, where FLT1, FLT2, and FLT3 divide the line into 4 equal sections.

Based on data in Table II, the threshold must be less than 0.28 to ensure detection of the 600 Ω grounding fault. On the other hand, the threshold must be higher than 0.23 to avoid false actions caused by noise. Therefore, 0.25 is selected as the threshold. When change rates exceed the threshold, protection starts. Then, the fault pole is selected according to the change amount of the IHD. Fault pole selection criterion is:

$$\begin{cases} \Delta H_{\mathrm{p}} > \Delta H_{\mathrm{n}}, & \text{Positive pole fault} \\ \Delta H_{\mathrm{n}} > \Delta H_{\mathrm{p}}, & \text{Negative pole fault} \end{cases} \tag{23}$$

where ΔH_{p} and ΔH_{n} are the IHD change values of positive pole and negative pole, respectively. The fault can be located based on moments where the change rates exceed threshold. According to (20) and (21), combined with the length of Line AB and Line BC, Δt is set as 0.01 ms and fault line selection criterion is calculated as:

$$\begin{cases} t_{\mathrm{C}} \geq t_{\mathrm{A}} - 1.24, & \text{Line AB fault} \\ t_{\mathrm{A}} \geq t_{\mathrm{C}} + 1.26, & \text{Line BC fault} \end{cases} \tag{24}$$

The proposed algorithm is effective to reduce the effects of abnormal data caused by noise or data error. However, to further avoid effects caused by noise, background noise needs to be detected and filtered during signal acquisition.

TABLE II
IHD CHANGE RATE PEAK TIME AND THE VALUE OF DIFFERENT FAULT TYPES WITHOUT NOISE AND WITH NOISE

Fault Type	Station	Peak Time (ms)	Peak Value (without noise)	Noise Peak (SNR = 40)
FLT1 600 Ω Grounding	A	0.7	0.28	0.18
	B	3.2	3.47	
	C	4.5	1.10	
FLT2 600 Ω Grounding	A	2.0	0.53	0.23
	B	2.0	1.74	
	C	3.2	0.38	
FLT3 600 Ω Grounding	A	3.2	0.70	0.23
	B	0.7	0.53	
	C	3.2	2.20	
FLT4 600 Ω Grounding	A	4.5	0.15	0.21
	B	0.7	0.32	
	C	0.7	0.47	

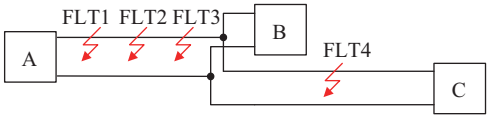

Fig. 7. Illustration of different fault points.

C. Verification Under Different Fault Types

Three fault cases are tested and analyzed in the following text to verify the proposed protection scheme.

1) Midpoint Fault of Line AB Positive Pole

When a grounding fault occurs at midpoint of Line AB positive pole, the energy function is applied to calculate energy level of each converter station. IHD value and its change rate are then calculated, which are shown in Fig. 8. The orange lines with marks indicate IHD values, blue lines indicate the change rate of IHD, and red dashed lines indicate the threshold of change rate.

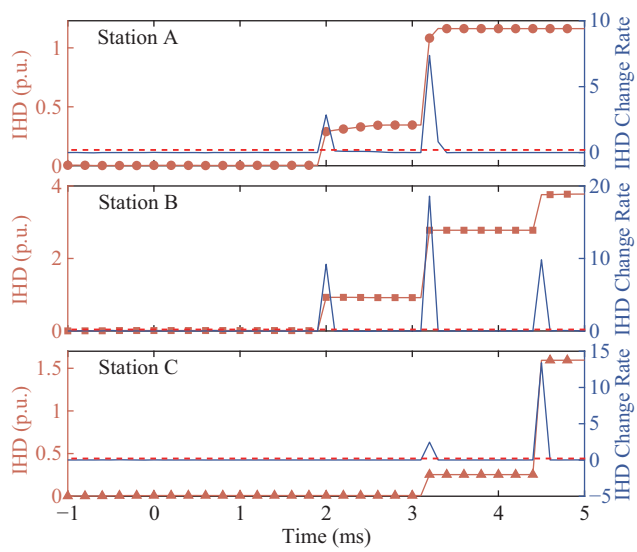

Fig. 8. IHD and its change rate of the midpoint fault on Line AB.

When a 600 Ω grounding fault occurs at the midpoint of Line AB, the IHD value and its change rate decrease, shown in Fig. 9.

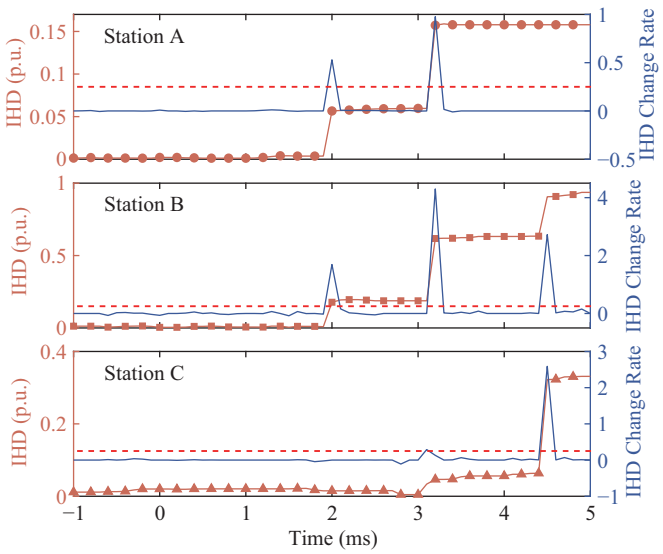

Fig. 9. IHD and its change rate of the midpoint 600 Ω fault on Line AB.

As shown in Fig. 8, the change rate of Station A exceeds the threshold at 2 ms, while the change rate of Station C exceeds the threshold at 3.2 ms. According to (24), the fault is located on Line AB when satisfying $t_{\mathrm{C}} \geq t_{\mathrm{A}} - 1.24$. For the case of a 600 Ω grounding fault shown in Fig. 9, the time points at which the change rates exceed the threshold are similar to those in Fig. 8; thus, the same conclusion can be drawn.

2) Midpoint Fault of Line BC Positive Pole

When a grounding fault occurs at the midpoint of Line BC positive pole, the IHD value and its change rate are shown in Fig. 10.

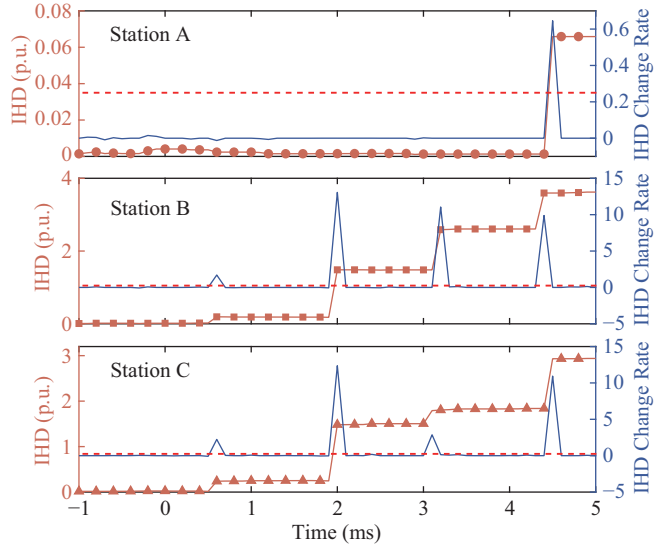

Fig. 10. IHD and its change rate of the midpoint fault on Line BC.

When a 600 Ω grounding fault occurs at the midpoint of Line BC, the IHD value and its change rate decrease, shown in Fig. 11.

As shown in Fig. 10, the change rate of Station C exceeds the threshold at 0.7 ms, while the change rate of Station A exceeds the threshold at 4.5 ms. According to (24), the fault is located on Line BC when satisfying $t_{\mathrm{A}} \geq t_{\mathrm{C}} + 1.26$. For the case of the 600 Ω grounding fault shown in Fig. 11, the change rate of Station A is still within the threshold after Station C exceeds the threshold by 1.26 ms, which can also locate the fault on Line BC.

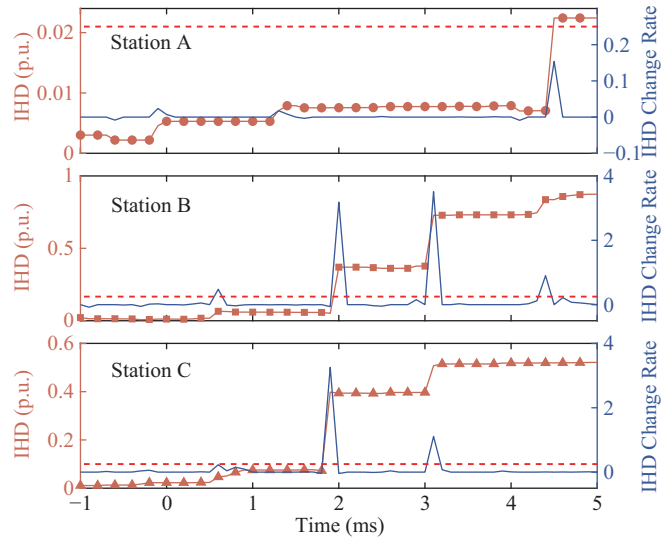

Fig. 11. IHD and its change rate of the midpoint 600 Ω fault on Line BC.

3) Faults at Different Fault Points of Line AB Positive Pole

The time that IHD change rate exceeds the threshold can also be applied to estimate the fault section on the fault line. Taking the grounding fault at different points on Line AB as an example, the IHD values with respect to distance and time of Station A and Station B are shown in Fig. 12. Fault location axis shows the distance between the fault point and Station A. As shown in Fig. 12, the IHD of the converter station closer to the fault point changes increasingly earlier. In contrast, the IHD of the converter station farther from the fault point rises later with a lower magnitude. Peak of the IHD for Station A is located at the fault point closer to Station A, while the peak of the IHD for Station B is located near Station B.

Based on the difference in time, the IHD change rates of Station A and Station B exceed the threshold, and the fault section can be estimated. A fault is set at FLT1, as shown in Fig. 7, and the IHD and its change rate at Station A and Station B are shown in Fig. 13.

As shown in Fig. 13, values of t_{A} and t_{B} in (22) are 0.7 ms and 2.0 ms, respectively, and distance x_{A} obtained by (22) is 241 km, which is close to the exact distance 233 km.

D. Discussion of Other Waveshape Similarity Algorithms

Abnormal data may cause distance value to be much higher than usual and may lead to protection maloperation. In this section, abnormal data is added to the energy data of the positive pole at Station A at −0.5 ms, i.e., 0.5 ms before the fault on Line AB positive pole occurs. Five different waveshape similarity algorithms are discussed and compared. Results are shown in Fig. 14.

As shown in Fig. 14(a), the IHD algorithm proposed can eliminate the effect of abnormal data. For two different waves,

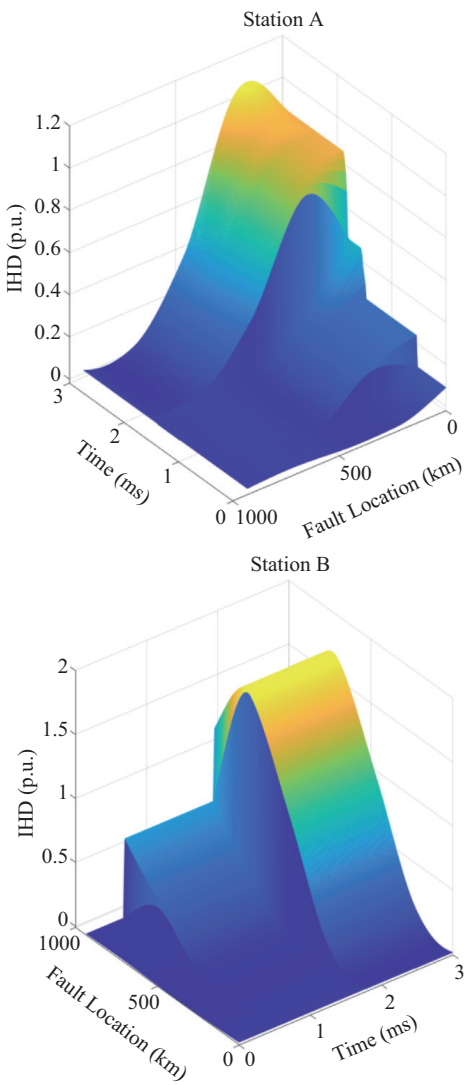

Fig. 12. IHD of the fault on Line AB with respect to the fault location and time.

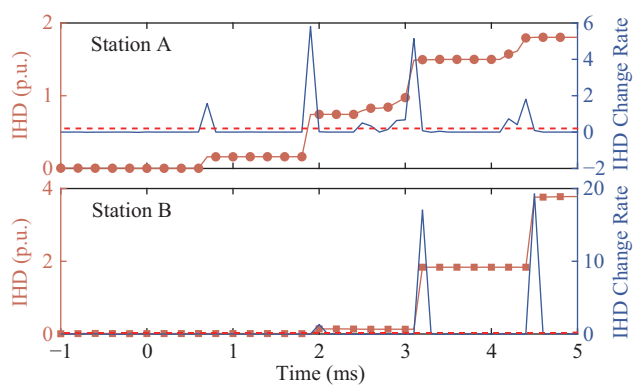

Fig. 13. IHD and its change rate of fault at FLT1 on Line AB.

calculating the absolute distance between the points as (25) can also reflect the similarity.

$$D_x(t) = |V_x(t) - V_{x0}(t)| \tag{25}$$

where $D_x(t)$ is the absolute distance between two waves at time t, $V_x(t)$ and $V_{x0}(t)$ are the energy levels of the present

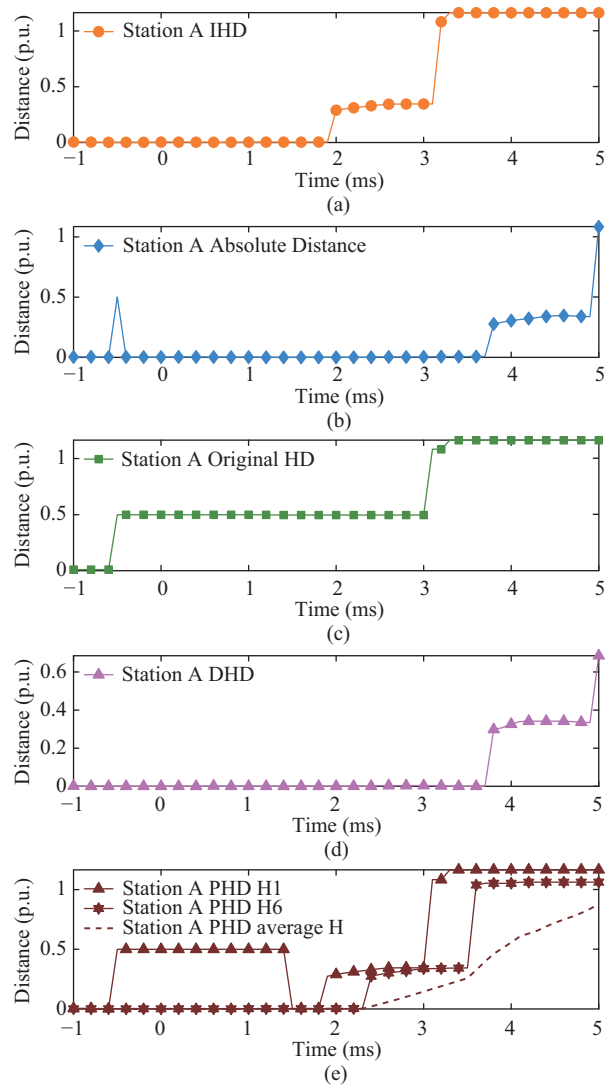

Fig. 14. Comparison of different waveshape similarity algorithms. (a) IHD algorithm. (b) Absolute distance algorithm. (c) Original HD algorithm. (d) DHD algorithm. (e) PHD algorithm.

state and the normal state, respectively. However, the absolute distance algorithm cannot eliminate the effect caused by the abnormal data and a peak emerges as shown in Fig. 14(b).

HD is a type of algorithm used to evaluate waveshape similarity, but the original HD algorithm is also easily affected by abnormal data. As shown in Fig. 14(c), the step emerges at 0.5 s, which is caused by abnormal data. To solve this problem, some improved HD algorithms have been proposed.

In [15], [16], similar to the IHD algorithm proposed in this paper, the directed HD D_i from W_1 to W_2 and the directed HD D_j from W_2 to W_1 are ranked in order from largest to smallest to obtain $D_{\mathrm{rank}i}$ and $D_{\mathrm{rank}j}$, respectively. Values of $D_{\mathrm{rank}i}/D_{\mathrm{rank}j}$ $(i = j = 1, 2, 3, \cdots)$ are calculated and compared with the set range to select maximum values of D_i and D_j. As shown in Fig. 14(d), the algorithm, which is named DHD here, can eliminate the effect of the abnormal data. However, compared with Fig. 14(a), the fault detection time point of the proposed IHD algorithm is much earlier than that of the DHD algorithm.

In [17], the PHD algorithm is proposed. In the algorithm, the larger one between $D_{\mathrm{rank}i}$ and $D_{\mathrm{rank}j}$ $(i = j)$ is selected as $H_{\mathrm{rank}i}$. Average value after removing the first 5 values of $H_{\mathrm{rank}i}$ is calculated and compared with the threshold to determine whether H_{rank1} or H_{rank6} will be selected as the maximum value. Results are shown in Fig. 14(e), where H1 and H6 are H_{rank1} and H_{rank6} respectively, average H is the average value of $H_{\mathrm{rank}i}$ without the first 5 values. As is shown in Fig. 14(e), a step emerges in H1 curve, and H6 curve is not affected by abnormal data. However, compared with Fig. 14(a) and H1 curve in Fig. 14(e), fault detection time of H6 curve is later, which means the sensitivity of using H_{rank6} as the maximum value is worse.

E. Advantages of Using Energy Function

When a grounding fault occurs on a DC line, amplitude of AC voltage and its phase angle at both ends of the line will also change rapidly. Combined with the proposed IHD method, the fault line can be theoretically discriminated by a single state parameter. However, compared with criterion of the energy level obtained by the energy function, the single-state parameter criterion cannot reflect overall energy level or operating states of the entire system. In other words, criterion using a single state parameter is not reliable because when a fault occurs, the single state parameter may not change significantly, which may cause the fault to not be detected and cleared accurately. In this section, we choose a fault occurring at the midpoint of Line AB positive pole as an example to verify the advantage of criterion applying the energy function. Simulation is performed using three criteria: energy level, AC voltage, and voltage phase. Results are shown in Fig. 15.

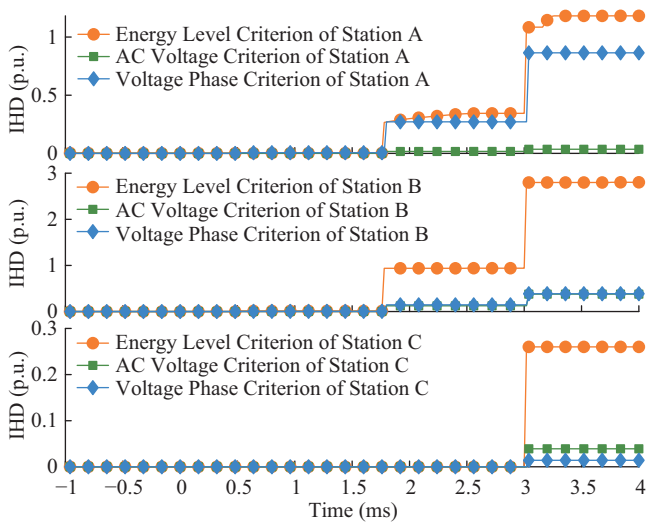

Fig. 15. Comparison of the energy level criterion and single state parameter criterion.

As shown in Fig. 15, IHD calculated using energy level criterion is larger than IHD of the other two criteria. A greater degree of variation means the energy level criterion is more sensitive and more effective at determining faults. Specifically, when using AC voltage as the criterion, only the IHD of Station B changes considerably to approximately 0.386 p.u., while the IHD of Station A and Station C only change to 0.035 p.u. and 0.039 p.u., respectively. The fault section cannot be determined correctly with the IHD of one station rising significantly. When using voltage phase as the criterion, the change in IHD at Station A is close to the counterpart of the energy level criterion. However, change in IHD at Station B is much smaller than IHD change of the energy level criterion. Therefore, it can be concluded that using energy level as a criterion of the protection scheme has advantages over using a single state parameter as the criterion.

F. Communication Delay Analysis and Comparison of Existing Methods

The sum of time taken by each process can be calculated using (26).

$$t_{\mathrm{total}} = t_{\mathrm{cal}} + t_{\mathrm{com}} + t_{\mathrm{act}} \tag{26}$$

where t_{cal} is time required to complete detection, which mainly includes time that the IHD change rate exceeds the threshold and time to complete the judgment. According to Table II, when a fault occurs near Station A (FLT1), there is $t_{\mathrm{A}} = 0.7$ ms < 1.24 ms, then the fault can be detected in 0.7 ms based on (24). When the fault occurs near Station B (FLT3), detection time is $t_{\mathrm{A}} = t_{\mathrm{C}} = 3.2$ ms, thus time t_{cal} ranges from 0.7 ms to 3.2 ms for faults at different locations. t_{com} is time spent on communication, including time to receive the signal of each converter station, time to return the action signal, and time delay, whose maxima are approximately 3.1 ms, 3.1 ms, and 10 ms, respectively. t_{act} is time for the DC circuit breaker to complete the opening process, which is approximately 2 ms. Maximum of t_{total} is approximately 21.4 ms, which can meet the requirement of backup protection for the UHVDC transmission system. Several backup protection schemes for the Wudongde ±800 kV three-terminal hybrid UHVDC transmission projects are introduced in [32], which are listed in Table III.

TABLE III
ACTION TIME OF DIFFERENT BACKUP PROTECTION SCHEMES

Backup Protection Scheme	Action Time (ms)
Current Differential Protection Scheme	1 100
Differential Current Energy Ratio Scheme	23.3
Undistorted Factor Scheme	22.2
Fault Current Similarity Scheme	20.1
Proposed Protection Scheme	21.4

The current differential protection scheme usually requires a delay time of 1100 ms to eliminate the impact of transient currents caused by line distribution capacitance, which cannot act rapidly. A differential current energy ratio scheme proposes a criterion by comparing the energy distribution of the differential current in the high- or low-frequency band. When the ratio of low-frequency current energy to high-frequency current energy is greater than 1, the fault is determined to be an internal fault; otherwise, it is determined to be an external fault. The undistorted factor is introduced in [32] to indicate the relationship between voltages of the measured point and fault point, thus identifying the internal fault or the external fault. A method for calculating the undistorted

factor is proposed in [32], which can eliminate the effect of line mode voltage at the fault point using a double-ended quantity. Although the two protection schemes mentioned above can effectively improve action speed, the requirement of communication synchronization is much higher. Fault current similarity scheme compares similarity of current waveforms on both sides of the line to determine internal fault and external fault. The scheme does not require strict communication synchronization, but it does require synchronous transmission of real-time current data, which requires high communication speed and stability. In contrast, the protection scheme proposed in this paper can effectively improve reliability because it only transmits the action signal and corresponding time point information.

V. Conclusion

To improve sensitivity and reliability for high-resistance grounding faults of a UHVDC transmission protection system, a protection scheme applying the DC system energy function and the IHD algorithm was proposed. A simulation model of the Wudongde ± 800 kV three-terminal hybrid UHVDC transmission project was applied to verify the proposed protection scheme. Simulation results showed the fault line was identified, and the fault section was estimated quickly and accurately by the proposed scheme, even in the case of a 600 Ω grounding fault. Moreover, other waveshape similarity algorithms and single-state parameter criteria were discussed and compared. Communication delay was analyzed and compared with existing protection schemes. Results showed the proposed method meets the time requirement of backup protection and improves speed and reliability by only transmitting the action signal and corresponding time point information.

References

[1] N. Fernandopulle and R. T. H. Alden, "Incorporation of detailed HVDC dynamics into transient energy functions," *IEEE Transactions on Power Systems*, vol. 20, no. 2, pp. 1043–1052, May 2005.

[2] M. Wang, T. An, H. Ergun, Y. L. Lan, B. Andersen, M. Szechtman, W. Leterme, J. Beerten, and D. V. Hertem, "Review and outlook of HVDC grids as backbone of transmission system," *CSEE Journal of Power and Energy Systems*, vol. 7, no. 4, pp. 797–810, Jul. 2021.

[3] M. Andreasson, D. V. Dimarogonas, H. Sandberg, and K. H. Johansson, "Distributed controllers for multiterminal HVDC transmission systems," *IEEE Transactions on Control of Network Systems*, vol. 4, no. 3, pp. 564–574, Sep. 2017.

[4] P. Bakas, L. Harnefors, S. Norrga, A. Nami, K. Ilves, F. Dijkhuizen, and H. P. Nee, "A review of hybrid topologies combining line-commutated and cascaded full-bridge converters," *IEEE Transactions on Power Electronics*, vol. 32, no. 10, pp. 7435–7448, Oct. 2017.

[5] J. Lu, X. M. Yuan, M. Q. Zhang, and J. B. Hu, "Supplementar Control for Mitigation of Successive Commutation Failures Considering the Influence of PLL Dynamics in LCC-HVDC Systems," *CSEE Journal of Power and Energy Systems*, vol. 8, no. 3, pp. 872–879, May. 2022.

[6] D. C. Tian, and X. F. Xiong, "Corrections of Original CFPREV Control in LCC-HVDC Links and Analysis of Its Inherent Plateau Effect," *CSEE Journal of Power and Energy Systems*, vol. 8, no. 1, pp. 10–16, Jan. 2022.

[7] N. Flourentzou, V. G. Agelidis, and G. D. Demetriades, "VSC-based HVDC power transmission systems: an overview," *IEEE Transactions on Power Electronics*, vol. 24, no. 3, pp. 592–602, Mar. 2009.

[8] A. Nami, J. Q. Liang, F. Dijkhuizen, and G. D. Demetriades, "Modular multilevel converters for HVDC applications: review on converter cells and functionalities," *IEEE Transactions on Power Electronics*, vol. 30, no. 1, pp. 18–36, Jan. 2015.

[9] S. Debnath, J. C. Qin, B. Bahrani, M. Saeedifard, and P. Barbosa, "Operation, control, and applications of the modular multilevel converter: A review," *IEEE Transactions on Power Electronics*, vol. 30, no. 1, pp. 37–53, Jan. 2015.

[10] H. Rao, C. Y. Zou, S. K. Xu, X. P. Cai, Y. Li, X. B. Zhao, Y. B. Zhou, Y. Yang, W. Wei, J. Chen, and T. L. Wei, "The On-site Verification of Key Technologies for Kunbei-Liuzhou-Longmen Hybrid Multi-terminal Ultra HVDC Project," *CSEE Journal of Power and Energy Systems*, vol. 8, no. 5, pp. 1281–1289, Sep. 2022.

[11] N. M. Haleem, A. D. Rajapakse, A. M. Gole, and I. T. Fernando, "Investigation of fault ride-through capability of hybrid VSC-LCC multi-terminal HVDC transmission systems," *IEEE Transactions on Power Delivery*, vol. 34, no. 1, pp. 241–250, Feb. 2019.

[12] X. Q. Chen, H. F. Li, Y. S. Liang, and G. Wang, "A protection scheme for hybrid multi-terminal HVDC networks utilizing a time-domain transient voltage based on fault-blocking converters," *International Journal of Electrical Power & Energy Systems*, vol. 118, no. 105825, Jan. 2020.

[13] X. Q. Chen, Y. S. Liang, G. Wang, H. F. Li, B. K. Li, and Z. Guo. "A control parameter analysis method based on a transfer function matrix of hybrid multi-terminal HVDC system with flexible adaptability for different operation modes," *International Journal of Electrical Power & Energy Systems*, vol. 116, no. 105584, Mar. 2020.

[14] F. Kong, Z. G. Hao, S. Zhang, and B. H. Zhang, "Development of a novel protection device for bipolar HVDC transmission lines," *IEEE Transactions on Power Delivery*, vol. 29, no. 5, pp. 2270–2278, Oct. 2014.

[15] G. F. Tang, X. Luo, and X. G. Wei, "Multi-terminal HVDC and dc-grid Technology," *Proceedings of the CSEE*, vol. 33, no. 10, pp. 8–17, Apr. 2013.

[16] C. H. Zhang, J. H. Huang, G. B. Song, and X. Z. Dong, "Non-unit ultra-high-speed line protection for multi-terminal hybrid LCC/MMC HVDC system and its application research," *IEEE Transactions on Power Delivery*, vol. 36, no. 5, pp. 2825–2838, Oct. 2021.

[17] Y. T. Wang, B. H. Zhang, and S. J. Cheng, "Pilot protection scheme for transmission line of a hybrid HVDC system based on polarity characteristics of current and voltage fault components," *The Journal of Engineering*, vol. 2019, no. 16, pp. 820–825, Mar. 2019.

[18] D. Wang, M. Q. Hou, M. Y. Gao and F. Qiao, "Travelling wave directional pilot protection for hybrid HVDC transmission line," International Journal of Electrical Power & Energy Systems, vol. 107, pp. 615–627, May 2019.

[19] L. Chen, Z. Q. Bo, X. N. Lin, F. R. Wei, M. Q. Yu, N. Jin, M. S. Khalid, Z. T. Li, J. G. Huang, and K. Deng, "Waveform similarity comparison based high-speed pilot protection for transmission line," Proceedings of the CSEE, vol. 37, no. 17, pp. 5018–5027, Sep. 2017,.

[20] L. Chen, X. N. Lin, Z. T. Li, F. R. Wei, H. Zhao, Z. Q. Bo, J. G. Huang, and K. Deng, "Similarity comparison based high-speed pilot protection for transmission line," *IEEE Transactions on Power Delivery*, vol. 33, no. 2, pp. 938–948, Apr. 2018.

[21] H. Zhao, X. N. Lin, K. Yu, H. Li, L. Chen, Z. T. Li, T. H. Wu, and Z. Q. Guo, "A high-speed protection scheme for HVDC transmission line based on hausdorff distance comparison," *Proceedings of the CSEE*, vol. 37, no. 23, pp. 6888–6900, Dec. 2017.

[22] X. L. Liu, A. H. Osman, and O. P. Malik, "Hybrid traveling wave/boundary protection for monopolar HVDC line," *IEEE Transactions on Power Delivery*, vol. 24, no. 2, pp. 569–578, Apr. 2009.

[23] F. Kong, Z. G. Hao, and B. H. Zhang, "Improved differential current protection scheme for CSC-HVDC transmission lines," *IET Generation, Transmission & Distribution*, vol. 11, no. 4, pp. 978–986, Mar. 2017.

[24] J. Liu, N. L. Tai, and C. J. Fan, "Transient-voltage-based protection scheme for dc line faults in the multiterminal VSC-HVDC system," *IEEE Transactions on Power Delivery*, vol. 32, no. 3, pp. 1483–1494, Jun. 2017.

[25] H. D. Chang, C. C. Chu, and G. Cauley, "Direct stability analysis of electric power systems using energy functions: theory, applications, and perspective," *Proceedings of the IEEE*, vol. 83, no. 11, pp. 1497–1529, Nov. 1995.

[26] T. Odun-Ayo and M. L. Crow, "Structure-preserved power system transient stability using stochastic energy functions," *IEEE Transactions on Power Systems*, vol. 27, no. 3, pp. 1450–1458, Aug. 2012.

[27] K. R. Padiyar and H. S. Y. Sastry, "A structure-preserving energy function for stability analysis of AC/DC systems," *Sadhana*, vol. 18, no. 5, pp. 787–799, Sep. 1993.

[28] N. Q. Jiang and H. D. Chiang, "Energy function for power system with detailed DC model: construction and analysis," *IEEE Transactions on Power Systems*, vol. 28, no. 4, pp. 3756–3764, Nov. 2013.

[29] G. Wang, J. B. Luo, H. F. Li, and Z. Q. Li, "Transient energy protection for ±800 kV UHVdc transmission lines," *Automation of Electric Power Systems*, vol. 34, no. 1, pp. 28–31, Jan. 2010.
[30] Z. H. Dai, N. N. Liu, C. Zhang, X. Y. Pan, and J. Y. Wang, "A pilot protection for HVDC transmission lines based on transient energy ratio of DC filter link," *IEEE Transactions on Power Delivery*, vol. 35, no. 4, pp. 1695–1706, Aug. 2020.
[31] L. L. Chen, X. Y. Pei, X. G. Wei, P. Z. Li, and G. F. Tang, "An effective ultra-high-speed identification scheme of lightning strokes suitable for VSC-based DC grids," *CSEE Journal of Power and Energy Systems*, doi: 10.17775/CSEEJPES.2021.04690.
[32] D. H. Zhang, C. J. Wu, J. H. He, and P. H. Ni, "A protection scheme for transmission line of LCC-MMC Hybrid HVDC system based on undistorted factor," *High Voltage Engineering*, vol. 48, no. 1, pp. 166–177, Jan. 2022.

Zijiang Wang received his B.Eng. degree in Electric Power System and Its Automation from Shandong University, Jinan, Shandong, China, in 2017, and his M.Eng. degree in Electrical Engineering from Zhengzhou University, Zhengzhou, Henan, China, in 2020. He is currently persuing the Ph.D. degree in the School of Electrical Engineering and Automation, Wuhan University, Wuhan, Hubei province, China. His main research interests include the protection and automation of UHVDC transmission system, the transient stability of power system.

Youping Fan received his Ph.D. degree in Control Theory and Control Engineering from Chongqing University, Chongqing, China, in 2003. He is currently a Professor of the School of Electrical Engineering and Automation, Wuhan University, Wuhan, China. His research interests are artificial intelligence and knowledge engineering, modeling and control of complex system, security analysis and risk control technology of power system, and parameter identification of power system.

Ben Shang received the B.Eng. degree in Electrical Engineering and Its Automation from Wuhan University, Wuhan, Hubei province, China, in 2019, where he is currently working torward the Ph.D. degree in Electrical Engineering. His research interests include power equipment fault diagnosis and state evaluation, machine learning, and pattern recognition.

Yinbiao Shu received his B.S. degree from North China Electric Power University in 1982, and his M.S. and Ph.D. degrees from the School of Electrical Engineering, Wuhan University in 2001 and 2007 respectively. He is a Professor of the Institute of Next Generation Power Systems & International Standards, Wuhan University, Wuhan, China. He has been engaged in research and development such as power grid dispatching and operation, power grid development and planning, research and construction of ultra-high voltage power transmission and smart grid, renewable energy development, and international operation, etc., with rich theoretical knowledge and practical experiences.